

TECHNICAL REPORT 1968  
February 2008

# Autonomous Underwater Vehicle Navigation

P. A. Miller  
SSC San Diego

J. Farrell  
Y. Zhao  
V. Djapic  
University of California, Riverside

Approved for public release;  
distribution is unlimited.



SSC San Diego  
San Diego, CA 92152-5001

# CONTENTS

<b>1</b>	<b>Introduction</b>	<b>1</b>
1.1	System Description . . . . .	1
1.2	Notation . . . . .	2
<b>2</b>	<b>Model Derivation</b>	<b>2</b>
<b>3</b>	<b>Navigation</b>	<b>4</b>
3.1	Inertial Measurement Unit . . . . .	6
3.2	Augmented System Equations . . . . .	6
3.3	Mechanization Equations . . . . .	7
3.4	Error State Equations . . . . .	7
3.5	Time Propagation . . . . .	9
3.6	Measurement Corrections . . . . .	9
3.6.1	Attitude Update . . . . .	10
3.6.2	Doppler Velocity Log Update . . . . .	11
3.6.3	Long Baseline Update . . . . .	12
3.6.4	Pressure Update . . . . .	14
<b>4</b>	<b>Analysis</b>	<b>15</b>
4.1	Incremental LBL Dropouts, Limited Compass Aiding . . . . .	17
4.2	Incremental DVL Beam Dropouts, No LBL Aiding . . . . .	19
<b>5</b>	<b>Experimental Results</b>	<b>21</b>
<b>6</b>	<b>Future Work</b>	<b>23</b>
<b>7</b>	<b>References</b>	<b>24</b>

## LIST OF FIGURES

1	Vehicle sensor configuration . . . . .	2
2	Long baseline interrogation cycle . . . . .	13
3	North–East plot of incremental LBL dropout scenario . . . . .	16
4	East position error $\tilde{\eta}_1(y)$ for incremental LBL dropout scenario . . . . .	17
5	Azimuth error $\tilde{\rho}(\psi)$ for incremental LBL dropout scenario . . . . .	18
6	Sound speed error $\tilde{c}$ for incremental LBL dropout scenario . . . . .	18
7	Velocity error $\tilde{v}_1(u)$ for incremental DVL dropout scenario . . . . .	19
8	Accelerometer bias error $\tilde{b}_a(u)$ for incremental DVL dropout scenario . . . . .	20
9	North, east, and down position error $\delta\eta_1$ standard deviation . . . . .	21
10	Long baseline transponder 1 residual . . . . .	22
11	Sound speed estimate $\hat{c}$ . . . . .	23
12	Semi-log plots of azimuth and gyro bias error standard deviations . . . . .	24
13	Accelerometer and gyro bias estimates . . . . .	25
14	Doppler velocity log beam 1 residual . . . . .	25

# EXECUTIVE SUMMARY

This report considers the vehicle navigation problem for an autonomous underwater vehicle with six degrees of freedom. We approach this problem using an error state formulation of the Kalman filter. Integration of the vehicle's high-rate inertial measurement unit's accelerometers and gyros allow time propagation while other sensors provide measurement corrections. The low-rate aiding sensors include a Doppler velocity log, an acoustic long baseline system that provides round-trip travel times from known locations, a pressure sensor for aiding depth, and an attitude sensor. Measurements correct the filter independently as they arrive, and as such, the filter is not dependent on the arrival of any particular measurement. The navigation system can estimate critical bias parameters that improve performance. The result is a robust navigation system. Simulation and experimental results are provided.

## 1. INTRODUCTION

With the emergence of inspection-class autonomous underwater vehicles, navigation and navigational accuracy are becoming increasingly important. Without an operator in the loop, the vehicle itself must use sensors to determine its location, orientation, and motion. Many of these unique sensors rely on acoustic measurements that present interesting challenges. The problem is how to effectively use all available sensor inputs to provide a continuous and robust estimate of the vehicle's navigational state.

One approach is to treat each sensor independently, each measuring a specific state. A position sensor measures position, a velocity sensor measures velocity, and so forth. This solution, however, is clearly not robust and does not take advantage of the kinematic relationships between states and measurements. Consider the situation where sensor performance degrades and measurement updates become sporadic. If position fixes are not regularly available, how should the position state evolve? One could dead-reckon with the velocity and heading, then blend this estimate with each position fix, but is this ad-hoc method optimal?

Here, we present an approach using an error state formulation of the Kalman filter to provide an optimal and robust solution to the vehicle navigation problem. This report concentrates on the application of the Kalman filter and development of the model and filter algorithms. It does not attempt to justify the Kalman filter [1, 2, 3] or make comparisons to other algorithms.

This report is an extension of previous work [4]. Here, we expand upon our approach and analysis, and reformulate algorithms to provide a more theoretically concrete implementation. The following section describes the system of interest. Section 2 develops the continuous-time model for this system, while Section 3 formulates the corresponding navigation equations. In Section 4, we choose several interesting scenarios to analyze critical aspects of our approach. The final two sections include experimental results and a discussion of potential future work.

### 1.1 SYSTEM DESCRIPTION

The particular system of interest is an underwater vehicle with six degrees of freedom. The vehicle propels itself via multiple thrusters, allowing for a variety of dynamic maneuvers. From a navigation standpoint, we assume that it can rotate and translate in any direction, by actuation or environmental disturbances. The vehicle's nominal operating speed is approximately 1 knot, and

it has an operating area on the order of  $100 \times 100 \text{ m}^2$  with a maximum depth of less than 50 m.

A unique suite of on-board sensors provide information related to the vehicle’s motion. The primary sensor is an inertial measurement unit that measures accelerations and angular rates in three dimensions. This sensor is reliable, but due to noise and unknown biases, it alone cannot provide sufficient navigational accuracy. Other sensors provide additional feedback. A Doppler velocity log provides velocities along four beam directions via acoustic Doppler measurements. An acoustic long baseline (LBL) system measures round-trip travel times between a transceiver on the vehicle and four transponder baseline stations at known locations. An attitude and pressure sensor complete the navigation suite. The attitude sensor provides orientation measurements, while the pressure sensor provides a sense of vehicle depth. We assume the platform-frame sensor locations are known exactly and that all measurements, except for the LBL, have negligible measurement latencies. Delay is inherent in the LBL system, and methods to address that delay to enhance navigation accuracy are a major contribution of this article. Figure 1 illustrates the general sensor configuration.

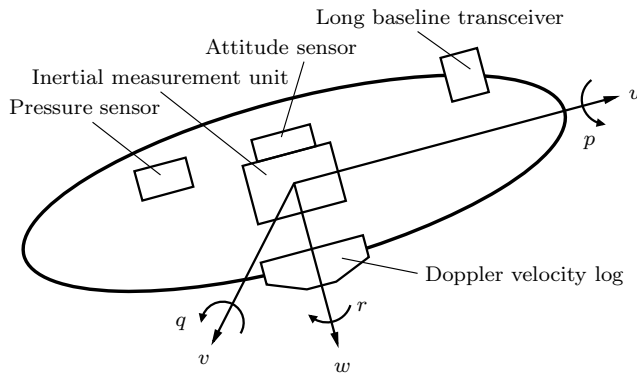


Figure 1: Vehicle sensor configuration.

## 1.2 NOTATION

We use the following notation [5]. For vehicle position and attitude, define tangent plane position  $\eta_1 = [x, y, z]^\top$  and attitude  $\eta_2 = [\phi, \theta, \psi]^\top$ . Vehicle position is defined in local tangent plane coordinates, where  $x$  aligns with north,  $y$  aligns with east, and  $z$  is down. Euler attitude angles are roll ( $\phi$ ), pitch ( $\theta$ ), and yaw ( $\psi$ ). In the vehicle or platform frame, define platform velocity  $\nu_1 = [u, v, w]^\top$ , angular rates  $\nu_2 = [p, q, r]^\top$ , and linear acceleration  $a^p = [a_u, a_v, a_w]^\top$ .

## 2. MODEL DERIVATION

Given limited knowledge of system dynamics and environmental uncertainties, a kinematic model is often preferable to a complex dynamic model. More importantly, kinematics are exact, with no uncertain parameters. Dynamics are not. This kinematic model relates platform accelerations, velocities, and angular rates to changes in tangent plane position and attitude. It does not account for vehicle or fluid dynamics, or other environmental forces, thus allowing the navigation algorithms to be platform independent.

The inertial frame of reference  $i$  is at the Earth center and is non-accelerating, non-rotating, and has no gravitational field. The Earth-center/Earth-fixed (ECEF) frame  $e$  is coincident with and rotates about the inertial frame at a known constant rate,  $\omega_{i/e}$ . On the surface of the Earth lies tangent frame  $t$ , which is fixed within the ECEF frame. The inertial acceleration expressed in the tangent frame is

$$a^i = R_t^i \left[ \Omega_{i/t}^t \Omega_{i/t}^t r^t + 2\Omega_{i/t}^t \dot{r}^t + \dot{\Omega}_{i/t}^t r^t + \ddot{r}^t \right],$$

where  $\Omega_{i/t}^t = [\omega_{i/t}^t \times]$  is the skew symmetric matrix form of rotation rate cross product of frame  $t$  with respect to frame  $i$ , represented in frame  $t$ . Vector  $r$  describes the vehicle position relative to the inertial origin. Solving for  $\ddot{r}^t$  yields

$$\begin{aligned} \ddot{r}^t &= R_i^t a^i - \Omega_{i/t}^t \Omega_{i/t}^t r^t - 2\Omega_{i/t}^t \dot{r}^t - \dot{\Omega}_{i/t}^t r^t \\ &= R_i^t (f^i + G^i) - \Omega_{i/t}^t \Omega_{i/t}^t r^t - 2\Omega_{i/t}^t \dot{r}^t - \dot{\Omega}_{i/t}^t r^t \\ &= f^t + (G^t - \Omega_{i/t}^t \Omega_{i/t}^t r^t) - 2\Omega_{i/t}^t \dot{r}^t - \dot{\Omega}_{i/t}^t r^t \\ &= f^t + g^t - 2\Omega_{i/e}^t \dot{r}^t, \end{aligned} \tag{1}$$

where vectors  $f$  and  $G$  represent the specific force and position dependent gravitational acceleration. Vector  $g^t$  is the local gravity vector. Note that  $\Omega_{i/t} = \Omega_{i/e} + \Omega_{e/t}$ , and  $\Omega_{e/t} \equiv 0$ .

We use an Euler attitude representation to describe vehicle orientation, where an Euler 3-2-1 rotation sequence [6] defines the relationship between tangent and platform frames. It is important to understand that each Euler angle describes a rotation about an axis in separate frames. We exploit this relationship between intermediate frames in the formulation of attitude rates and in the measurement correction of attitude angles. The combined rotation sequence from tangent frame  $t$  to platform frame  $p$  is

$$\begin{aligned} R_t^p &= R_1(\phi)R_2(\theta)R_3(\psi) \\ &= \begin{bmatrix} c\theta c\psi & c\theta s\psi & -s\theta \\ c\psi s\theta s\phi - c\phi s\psi & c\phi c\psi + s\theta s\phi s\psi & c\theta s\phi \\ c\phi c\psi s\theta + s\phi s\psi & -c\psi s\phi + c\phi s\theta s\psi & c\theta c\phi \end{bmatrix}, \end{aligned}$$

with inverse  $R_p^t = (R_t^p)^{-1} = (R_t^p)^\top$ . The velocity vectors in platform and tangent frames are related by  $v^t = R_p^t v^p$  and

$$v^p = R_t^p v^t. \tag{2}$$

The time derivative of the second equation is

$$\begin{aligned} \dot{v}^p &= R_t^p \dot{v}^t + \dot{R}_t^p v^t \\ &= R_t^p (f^t + g^t - 2\Omega_{i/e}^t v^t) + (-\Omega_{t/p}^p R_t^p) R_p^t v^p \\ &= a^p - 2\Omega_{i/e}^p v^p - (\Omega_{i/p}^p - \Omega_{i/e}^p) v^p \\ &= a^p - R_t^p \Omega_{i/e}^t R_p^t v^p - \Omega_{i/p}^p v^p, \end{aligned} \tag{3}$$

where we have expressed  $\dot{v}^t$  in the inertial frame using equation (1). Angular rate  $\Omega_{i/p}^p$  is computed from the gyro measurement by removing biases. Platform acceleration  $a^p$  is computed directly from the accelerometer specific force measurement by compensating for gravity and removing biases.

Recall that each Euler angle defines a rotation about an axis in separate frames. To relate the Euler attitude rates  $(\dot{\phi}, \dot{\theta}, \dot{\psi})$  to angular rates in the platform frame, relate rotation axes  $(\hat{i}_1, \hat{j}_2, \hat{k}_3)$

in their respective intermediate frames to platform frame coordinates  $(\hat{i}_p, \hat{j}_p, \hat{k}_p)$ . For example,  $[\hat{i}_p, \hat{j}_p, \hat{k}_p]^\top = R_2^\top(\theta)R_1^\top(\psi)[\hat{i}_2, \hat{j}_2, \hat{k}_2]^\top$ . Let

$$\begin{aligned}\omega_{t/p}^p &= \dot{\phi}\hat{i}_1 + \dot{\theta}\hat{j}_2 + \dot{\psi}\hat{k}_3 \\ &= \dot{\phi}\hat{i}_p + \dot{\theta}(c\phi\hat{j}_p - s\phi\hat{k}_p) - \dot{\psi}(s\theta\hat{i}_p - c\theta s\phi\hat{j}_p - c\theta c\phi\hat{k}_p) \\ &= (\dot{\phi} - \dot{\psi}s\theta)\hat{i}_p + (\dot{\theta}c\phi + \dot{\psi}c\theta s\phi)\hat{j}_p + (\dot{\psi}c\theta c\phi - \dot{\theta}s\phi)\hat{k}_p\end{aligned}$$

be the vector expression of angular rates in platform frame  $p$  relative to the tangent frame  $t$ , represented in frame  $p$ . In matrix form and using notation from Section 1.2, the Euler and platform angular rates are related by  $\nu_2 = \Omega\dot{\eta}_2$  and

$$\dot{\eta}_2 = \Omega^{-1}\nu_2, \quad (4)$$

where  $\nu_2 = \omega_{t/p}^p = \omega_{i/p}^p - \omega_{i/e}^p$ ,  $\dot{\eta}_2 = [\dot{\phi}, \dot{\theta}, \dot{\psi}]^\top$ , and

$$\Omega = \begin{bmatrix} 1 & 0 & -s\theta \\ 0 & c\phi & c\theta s\phi \\ 0 & -s\phi & c\theta c\phi \end{bmatrix}.$$

Note that the inverse relationship approaches a singularity as  $\theta \rightarrow \pm\frac{\pi}{2}$ . It is assumed the vehicle will not operate near this singularity. If operation near  $\pm\frac{\pi}{2}$  is desired, then an alternative attitude representation, such as quaternions, would remove this singularity.

After equations (2)–(4) are summarized using the notation from Section 1.2, the continuous-time kinematic model is

$$\begin{aligned}\dot{\eta}_1 &= R_p^t \nu_1 \\ \dot{\eta}_2 &= \Omega^{-1} \nu_2 \\ \dot{\nu}_1 &= a^p - R_t^p \Omega_{i/e}^t R_p^t \nu_1 - \Omega_{i/p}^p \nu_1.\end{aligned} \quad (5)$$

The next section utilizes this model, along with bias and measurement models, to propagate the system through time and formulate measurement predictions.

### 3. NAVIGATION

Given system output  $y$ , we wish to reconstruct the entire internal state  $x$ . From linear systems theory, we know that if the discrete system

$$\begin{aligned}x_{k+1} &= \Phi x_k + \Gamma \omega_k \\ y_k &= H x_k\end{aligned}$$

is observable, then we can design the observer

$$\begin{aligned}\hat{x}_{k+1} &= \Phi \hat{x}_k + L(y_k - \hat{y}_k) \\ \hat{y}_k &= H \hat{x}_k\end{aligned}$$

such that the eigenvalues of  $(\Phi - LH)$  lie within the unit circle. This condition is necessary for asymptotic stability of the error state system, defined by

$$\begin{aligned}\delta x_{k+1} &= (\Phi - LH)\delta x_k \\ \delta y_k &= H\delta x_k.\end{aligned}$$

Asymptotic stability of the error state system causes  $\delta x_k$  to converge exponentially to zero, thereby estimating  $x_k$ . We use notation  $\delta x_k$ , as opposed to  $\tilde{x}_k$ , to indicate the expected value of the error rather than the true error. For time-varying systems,  $L_k$  must stabilize  $(\Phi_k - L_k H_k)$  for all time [7, 8].

Here, we employ the Kalman filter to design  $L_k$  in an optimal manner, given noisy measurements  $y$ . The Kalman filter is optimal in the mean-squared sense [1, 2, 3]. In the following sections, we formulate system error state equations and apply the Kalman filter. Our formulation revolves around the system's inertial measurement unit (IMU), and as such, we describe this sensor first in Section 3.1. Section 3.2 defines the augmented system equations. These equations model the true system, while Section 3.3 defines the mechanization equations that provide the navigation state vector  $\hat{x}$ . The difference between the actual and mechanized systems is the error state system. A model for the error state system is described in Section 3.4. We use the error state system to design the Kalman filter. Section 3.5 applies the Kalman filter time propagation equations

$$\delta x_{k+1}^- = \Phi_k \delta x_k^- \quad (6)$$

$$P_{k+1}^- = \Phi_k P_k^- \Phi_k^\top + Q_d, \quad (7)$$

where equation (6) propagates the error state  $\delta x$  and equation (7) propagates the error state covariance  $P_k$ . Section 3.6 applies the Kalman filter measurement correction equations

$$K_k = P_k^- H_k^\top (H_k P_k^- H_k^\top + R_k)^{-1} \quad (8)$$

$$\delta y_k = y_k - h(\hat{x}_k) \quad (9)$$

$$\delta x_k^+ = \delta x_k^- + K_k (\delta y_k - H_k \delta x_k^-) \quad (10)$$

$$P_k^+ = (I - K_k H_k) P_k^-, \quad (11)$$

to the aiding sensors. Equation (8) computes the optimal Kalman gain, equation (9) computes the measurement residual, equation (10) corrects the error state estimate, and equation (11) updates the error state covariance matrix. Circular (i.e., angular) measurements should correct the innovation  $(\delta y_k - H \delta x_k^-)$  to lie on interval  $[-\pi, \pi)$ . Superscript  $-$  indicates the *a priori* state or covariance at time  $k$  immediately prior to the innovation. Superscript  $+$  indicates the *a posteriori* state or covariance at time  $k$  immediately after the innovation. Kalman gain  $K_k$  is the optimal observer gain  $L_k$  at instant  $k$ . After a measurement correction, the filter should initialize the *a priori* state and covariance to the *a posteriori* state and covariance for the next filter iteration (i.e.,  $\hat{x}_{k+1}^- = \hat{x}_k^+$  and  $\hat{P}_{k+1}^- = \hat{P}_k^+$ ).

Recognizing the difference between the error state  $\delta x$  and navigation state  $\hat{x}$  is important. The navigation mechanization computes  $\hat{x}$  by integration of the IMU data between time instants  $t_k$  and  $t_{k+1}$ , at which aiding measurements are available. At such time instants,  $\hat{x}$  is used to predict the measurement. The filter uses the residual between the actual and predicted measurements to estimate  $\delta x^+$ . When  $\delta x^+$  is available, the navigation state  $\hat{x}$  correction is

$$\hat{x}^+ = \hat{x}^- + \delta x^+. \quad (12)$$

After each navigation state correction, error states  $\delta x^-$  and  $\delta x^+$  are zero since the navigation state estimate now incorporates this information. Clearly, if we correct  $\hat{x}$  immediately after each  $\delta x$  correction,  $\delta x^-$  is always zero, and it is not necessary to propagate  $\delta x^-$  as in equation (6).

### 3.1 INERTIAL MEASUREMENT UNIT

The inertial measurement unit (IMU) is the primary high-rate sensor. It measures linear accelerations via accelerometers and angular rates via fiber-optic gyros. The IMU effective measurement point defines the origin of the platform frame. The IMU also provides an accurate time measurement since the last update. This delta time measurement is useful for precise integration, later described in Section 3.5. We expect this sensor to provide continuous updates without interruption.

The accelerometer specific force and gyro measurement outputs,  $y_a$  and  $y_g$ , respectively, are modeled by

$$y_a = a^p - R_t^p g^t + b_a + n_a \quad (13a)$$

$$y_g = \omega_{i/p}^p + b_g + n_g, \quad (13b)$$

where  $(b_a, n_a)$  and  $(b_g, n_g)$  are bias and noise vectors. Noise vectors  $n_a$  and  $n_b$  are distributed according to  $N(0, \sigma_a^2 I)$  and  $N(0, \sigma_b^2 I)$ , respectively, and are assumed to be white noise processes [1]. The acceleration and angular rate estimates are computed as

$$\hat{a}^p = y_a + \hat{R}_t^p g^t - \hat{b}_a \quad (14a)$$

$$\hat{\omega}_{i/p}^p = y_g - \hat{b}_g. \quad (14b)$$

Bias vectors  $b_a$  and  $b_g$  are modeled as random constants plus random walks, where

$$\dot{b}_a = \omega_a \quad \dot{\hat{b}}_a = 0 \quad (15a)$$

$$\dot{b}_g = \omega_g \quad \dot{\hat{b}}_g = 0. \quad (15b)$$

The driving noise vectors  $\omega_a$  and  $\omega_g$  are distributed according to  $N(0, \sigma_{ba}^2 I)$  and  $N(0, \sigma_{bg}^2 I)$ , respectively.

### 3.2 AUGMENTED SYSTEM EQUATIONS

Augmenting our continuous-time model, in equation (5), with the models for the unknown parameters in equations (15a) and (15b), yields the system state vector

$$x = [ \eta_1^\top \quad \eta_2^\top \quad \nu_1^\top \quad b_a^\top \quad b_g^\top \quad c ]^\top.$$

The additional parameter  $c$  represents our estimate for the speed of sound in seawater. We model  $c$  as a random constant plus random walk with driving noise  $\omega_c \sim N(0, \sigma_c^2)$ , where  $\sigma_c = 0.1$  m/s. This estimate is necessary to calculate round-trip distances from travel times for the long baseline system, described in Section 3.6.3. The process noise input vector is

$$u = [ n_a^\top \quad n_g^\top \quad \omega_a^\top \quad \omega_g^\top \quad \omega_c ]^\top,$$

where all quantities are mutually uncorrelated, Gaussian, white noise vectors. The augmented true system equations are therefore

$$\begin{aligned} \dot{\eta}_1 &= R_p^t \nu_1 \\ \dot{\eta}_2 &= \Omega^{-1}(y_g - b_g - n_g - R_t^p \omega_{i/e}^t) \\ \dot{\nu}_1 &= (y_a + R_t^p g^t - b_a - n_a) - R_t^p \Omega_{i/e}^t R_p^t \nu_1 - (y_g - b_g - n_g) \times \nu_1 \\ \dot{b}_a &= \omega_a \\ \dot{b}_g &= \omega_g \\ \dot{c} &= \omega_c, \end{aligned} \quad (16)$$

where we have substituted for  $a^p$  and  $\nu_2$  with equations (14a) and (14b), respectively, in preparation for the development of the error state equations in Section 3.4.

### 3.3 MECHANIZATION EQUATIONS

The mechanization equations represent the expected value of the true system. Our estimate of the true system, equation (16), is

$$\begin{aligned}
\dot{\hat{\eta}}_1 &= \hat{R}_p^t \hat{\nu}_1 \\
\dot{\hat{\eta}}_2 &= \hat{\Omega}^{-1}(y_g - \hat{b}_g - \hat{R}_t^p \omega_{i/e}^t) \\
\dot{\hat{\nu}}_1 &= (y_a + \hat{R}_t^p g^t - \hat{b}_a) - \hat{R}_t^p \Omega_{i/e}^t \hat{R}_t^p \hat{\nu}_1 - (y_g - \hat{b}_g) \times \hat{\nu}_1 \\
\dot{\hat{b}}_a &= 0 \\
\dot{\hat{b}}_g &= 0 \\
\dot{\hat{c}} &= 0,
\end{aligned} \tag{17}$$

where we assume the gravitation vector  $g^t$  and rotation rate  $\Omega_{i/e}^t$  are deterministic.

### 3.4 ERROR STATE EQUATIONS

The error state equations represent the expected value of the error between the true system and its estimate,  $\delta \dot{x} = \dot{x} - \dot{\hat{x}}$ . To compute the transformation error between two rotation matrices, we define a small-angle transformation as  $\hat{R}_p^t = (I - [\delta\rho \times])R_p^t$ , where  $(I - [\delta\rho \times])$  represents a small-angle transformation from the true tangent frame to the computed tangent frame [9]. The quantity  $\delta\rho$  represents the small-angle error between true and computed frames. The error state vector is then

$$\delta x = [ \delta\eta_1^\top \quad \delta\rho^\top \quad \delta\nu_1^\top \quad \delta b_a^\top \quad \delta b_g^\top \quad \delta c ]^\top, \tag{18}$$

where  $\delta\rho$  replaces  $\delta\eta_2$ . The following relations are useful in the subsequent analysis;

$$\hat{R}_p^t = (I - [\delta\rho \times])R_p^t \tag{19a}$$

$$R_p^t = (I + [\delta\rho \times])\hat{R}_p^t \tag{19b}$$

$$\hat{R}_t^p = R_t^p(I + [\delta\rho \times]) \tag{19c}$$

$$R_t^p = \hat{R}_t^p(I - [\delta\rho \times]). \tag{19d}$$

Using the small-angle relationships, we compute the error state equations for each state. The tangent position error is

$$\begin{aligned}
\delta\dot{\eta}_1 &= \dot{\eta}_1 - \dot{\hat{\eta}}_1 \\
&= \hat{R}_p^t \delta\nu_1 + [\delta\rho \times] \hat{R}_p^t \delta\nu_1 + [\delta\rho \times] \hat{R}_p^t \hat{\nu}_1 \\
&\approx \hat{R}_p^t \delta\nu_1 - [\hat{R}_p^t \hat{\nu}_1 \times] \delta\rho,
\end{aligned} \tag{20}$$

where we have manipulated the terms such that the error state coefficients can be represented in matrix form. To determine the error state model for  $\delta\dot{\rho}$  [10], differentiate the rotation matrix error  $\delta R_p^t = [\delta\rho \times]R_p^t$ ,

$$\begin{aligned}
\delta\dot{R}_p^t &= [\delta\dot{\rho} \times]R_p^t + [\delta\rho \times]\dot{R}_p^t \\
&= [\delta\dot{\rho} \times]R_p^t + [\delta\rho \times](R_p^t \Omega_{i/p}^p),
\end{aligned}$$

and solve for  $[\delta\dot{\rho}\times]$ ,

$$\begin{aligned}
[\delta\dot{\rho}\times] &= (\dot{R}_p^t - \hat{R}_p^t)R_t^p - [\delta\rho\times]R_p^t\Omega_{t/p}^p R_t^p \\
&= (R_p^t\Omega_{t/p}^p - \hat{R}_p^t\hat{\Omega}_{t/p}^p)R_t^p - [\delta\rho\times]\Omega_{t/p}^t \\
&= \Omega_{t/p}^t - \hat{R}_p^t\hat{\Omega}_{t/p}^p\hat{R}_t^p(I - [\delta\rho\times]) - [\delta\rho\times]\Omega_{t/p}^t \\
&\approx \Omega_{t/p}^t - \hat{\Omega}_{t/p}^t + \hat{\Omega}_{t/p}^t[\delta\rho\times] - [\delta\rho\times]\hat{\Omega}_{t/p}^t.
\end{aligned}$$

Equivalently, this expression written in vector form is

$$\begin{aligned}
\delta\dot{\rho} &= \omega_{t/p}^t - \hat{\omega}_{t/p}^t + \hat{\omega}_{t/p}^t \times \delta\rho \\
&= R_p^t\omega_{i/p}^p - \hat{R}_p^t\hat{\omega}_{i/p}^p - \delta\omega_{i/t}^t + (\hat{R}_p^t\hat{\omega}_{i/p}^p - \hat{\omega}_{i/t}^t) \times \delta\rho \\
&= \hat{R}_p^t\delta\omega_{i/p}^p + [\delta\rho\times]\hat{R}_p^t\delta\omega_{i/p}^p - \delta\omega_{i/t}^t - \hat{\omega}_{i/t}^t \times \delta\rho \\
&\approx \hat{R}_p^t(-\delta b_g - n_g) - \delta\omega_{i/t}^t - \hat{\omega}_{i/t}^t \times \delta\rho,
\end{aligned} \tag{21}$$

where  $\delta\omega_{i/t}^t = \{-\omega_{i/e}[\sin\bar{\phi}, 0, \cos\bar{\phi}]^\top \partial\bar{\phi}/\partial\eta_1\}\delta\eta_1$  and  $\bar{\phi}$  is the vehicle latitude. The platform velocity error is

$$\begin{aligned}
\delta\dot{\nu}_1 &= \dot{\nu}_1 - \hat{\nu}_1 \\
&\approx \hat{R}_t^p \left\{ [g^t \times] + \omega_{i/e}^t (\hat{R}_p^t \hat{\nu}_1)^\top - (\omega_{i/e}^t \cdot \hat{R}_p^t \hat{\nu}_1) I \right\} \delta\rho \\
&\quad - \left\{ [(y_g - \hat{b}_g) \times] + \hat{R}_t^p \Omega_{i/e}^t \hat{R}_p^t \right\} \delta\nu_1 - \delta b_a - n_a \\
&\quad - [\hat{\nu}_1 \times] \delta b_g - [\hat{\nu}_1 \times] n_g + \hat{R}_t^p \delta g^t + \hat{R}_t^p [\hat{R}_p^t \hat{\nu}_1 \times] \delta\omega_{i/e}^t.
\end{aligned} \tag{22}$$

Remaining error expressions for  $\delta b_a$ ,  $\delta b_g$ , and  $\delta c$  are trivial and, as such, their derivation is not shown. The resulting continuous-time error state system is

$$\delta\dot{x} = F\delta x + Gu, \tag{23}$$

where

$$F = \begin{bmatrix} 0 & -[\hat{R}_p^t \hat{\nu}_1 \times] & \hat{R}_p^t & 0 & 0 & 0 \\ F_{21} & -\Omega_{i/e}^t & 0 & 0 & -\hat{R}_p^t & 0 \\ F_{31} & F_{32} & F_{33} & -I & -[\hat{\nu}_1 \times] & 0 \\ 0 & 0 & 0 & 0 & 0 & 0 \\ 0 & 0 & 0 & 0 & 0 & 0 \\ 0 & 0 & 0 & 0 & 0 & 0 \end{bmatrix}$$

$$F_{21} = \partial\omega_{i/t}^t/\partial\eta_1$$

$$F_{31} = \hat{R}_t^p \left\{ \partial g^t/\partial\eta_1 + [\hat{R}_p^t \hat{\nu}_1 \times] \partial\omega_{i/e}^t/\partial\eta_1 \right\}$$

$$F_{32} = \hat{R}_t^p \left\{ [g^t \times] + \omega_{i/e}^t (\hat{R}_p^t \hat{\nu}_1)^\top - (\omega_{i/e}^t \cdot \hat{R}_p^t \hat{\nu}_1) I \right\}$$

$$F_{33} = -[(y_g - \hat{b}_g) \times] - \hat{R}_t^p \Omega_{i/e}^t \hat{R}_p^t$$

and

$$G = \begin{bmatrix} 0 & 0 & 0 & 0 & 0 \\ 0 & -\hat{R}_p^t & 0 & 0 & 0 \\ -I & -[\hat{\nu}_1 \times] & 0 & 0 & 0 \\ 0 & 0 & I & 0 & 0 \\ 0 & 0 & 0 & I & 0 \\ 0 & 0 & 0 & 0 & I \end{bmatrix}.$$

Due to the relatively small operating area, we assume  $F_{21}$  and  $F_{31}$  are approximately zero. Note that the error state vector contains  $\delta\rho$ , while the navigation state contains  $\eta_2$ . The measurement correction routines in Section 3.6 will account for the use of  $\delta\rho$ .

### 3.5 TIME PROPAGATION

The time propagation routine propagates the navigation state, error state, and error state covariance through time. For each measurement update from the IMU, the time propagation routine computes the continuous-time system, the discrete-time system, and then propagates the system state and covariance. The continuous-time system is  $F$  and  $G$  with process noise distribution matrix  $Q$ , where matrices  $F$  and  $G$  are computed according to equation (23) and  $Q = E\langle uu^\top \rangle$ . We assume  $Q = \text{diag}(\sigma_a^2 I, \sigma_b^2 I, \sigma_{ba}^2 I, \sigma_{bg}^2 I, \sigma_c^2)$ . To compute the equivalent discrete-time system, we compute the matrix exponential

$$\Upsilon = \exp \left( \begin{bmatrix} -F & GQG^\top \\ 0 & F^\top \end{bmatrix} \Delta t \right)$$

using algorithms from reference [11]. Quantity  $\Delta t$  is the integration period from the IMU. The result is

$$\Upsilon = \begin{bmatrix} -D & \Phi^{-1}Q_d \\ 0 & \Phi^\top \end{bmatrix},$$

where matrices  $\Phi$  and  $Q_d$  represent the discrete-time system [12]. Matrix  $\Phi(k+1, k)$  propagates the error state  $\delta x_k^-$  and covariance  $P_k^-$ , where  $P_k^- = E\langle \delta x_k^- \delta x_k^{-\top} \rangle$ , from time  $k$  to  $k+1$  according to equations (6) and (7), respectively. Matrix  $Q_d$  represents the discrete-time process noise distribution matrix at time  $k$ , and  $D$  is a nonzero dummy matrix. Given  $\Upsilon$ , matrices  $\Phi$  and  $Q_d$  are trivially solved from its sub-matrices,

$$\Phi(k+1, k) = \Upsilon[n+1:2n, n+1:2n]^\top \quad (24)$$

$$Q_d(k) = \Phi(k+1, k)\Upsilon[1:n, n+1:2n], \quad (25)$$

where  $\Upsilon[r_1:r_2, c_1:c_2]$  represents rows  $r_1$  through  $r_2$  and columns  $c_1$  through  $c_2$  of the  $2n \times 2n$  matrix  $\Upsilon$ .

We propagate the navigation state estimate  $\hat{x}^-$  using a predictor-corrector integration algorithm [13],

$$\begin{aligned} x_{k+1}^p &= x_k^- + f(x_k^-, y_k)\Delta t \\ x_{k+1}^c &= x_k^- + f(x_{k+1}^p, y_k)\Delta t \\ x_{k+1}^- &= \frac{1}{2}(x_{k+1}^p + x_{k+1}^c), \end{aligned} \quad (26)$$

where  $y_k = [y_a(k), y_g(k)]^\top$ , then correct the resulting attitude angles to lie on interval  $[-\pi, \pi)$ . Function  $f(x, y)$  is the continuous-time mechanization described in equation (17).

### 3.6 MEASUREMENT CORRECTIONS

In this section, we use the terms *sensor* and *measurement* to refer to all sensors other than the IMU. These aiding sensors are discussed in Sections 3.6.1 through 3.6.4. Each sensor runs independent of the next, with its own update rate and performance characteristics. Thus, measurement corrections are asynchronous. As a measurement arrives, it is evaluated and then incorporated into the error state estimate. If a measurement does not arrive, no calculations are necessary. The algorithm does

not wait for or expect measurements to arrive in an ordered fashion; the error state and navigation state will propagate according to equations (6) and (26), respectively, via the IMU data, with or without measurement corrections.

Measurements are evaluated with several sanity checks. One such check verifies that the measurement lies within three standard deviations of its estimate,  $(\delta y_k - H_k \delta x_k^-)^2 < 9(H_k P_k^- H_k^\top + R_k)$ , where  $\delta y_k$  is the measurement residual and matrix  $(H_k P_k^- H_k^\top + R_k)$  represents the measurement covariance. Additional logic is necessary to help ensure that this algorithm does not disregard valid measurements, especially upon initialization.

Valid measurements correct the error state estimate according to equation (10). The following sections describe the low-rate aiding sensors and their respective measurement correction. Measurement corrections require a measurement residual  $\delta y$ , sensor output matrix  $H$ , and measurement noise matrix  $R$  to evaluate equations (8) and (10). Note that the error state vector contains  $\delta \rho$ , while the navigation state vector contains  $\hat{\eta}_2$ . We cannot simply correct the attitude states of  $\hat{x}$ , as described in equation (12). Instead, we use  $\hat{\eta}_2^-$  to correct transformation matrix  $\hat{R}_t^p$  via (19d), where

$$\hat{R}_t^p(\hat{\eta}_2^+) = \hat{R}_t^p(\hat{\eta}_2^-)(I - [\delta \rho \times]), \quad (27)$$

and compute  $\hat{\eta}_2^+$  from the resulting transformation matrix,

$$\hat{\phi}^+ = \arctan2\left(\hat{R}_t^p[2, 3], \hat{R}_t^p[3, 3]\right) \quad (28a)$$

$$\hat{\theta}^+ = -\arctan\left(\frac{\hat{R}_t^p[1, 3]}{\sqrt{1 - \left(\hat{R}_t^p[1, 3]\right)^2}}\right) \quad (28b)$$

$$\hat{\psi}^+ = \arctan2\left(\hat{R}_t^p[1, 2], \hat{R}_t^p[1, 1]\right), \quad (28c)$$

where  $\hat{R}_t^p[i, j]$  represents the  $(i, j)$  element of matrix  $\hat{R}_t^p(\hat{\eta}_2^+)$  [12]. Function  $\arctan2(y, x)$  is the four-quadrant arc tangent function. To ensure numerical stability, it is necessary to normalize  $\hat{R}_t^p$  prior to evaluating equations (28a)–(28c).

### 3.6.1 Attitude Update

The attitude sensor combines four tilt and three magnetometer measurements to produce roll, pitch, and yaw information. We assume the vehicle dynamics are slow, and as such, the coupling between the inclinometers and platform acceleration is negligible. We also assume the magnetometer is calibrated to compensate for hard iron characteristics of the operating region. Momentary magnetic spikes can easily be ignored. The sensor model is

$$y_e = \eta_2 + n_e,$$

where sensor noise  $n_e$  is distributed according to  $N(0, \sigma_e^2 I)$ . We can predict the measurement as

$$\hat{y}_e = \hat{\eta}_2,$$

and compute the measurement residual as

$$\delta y_e = y_e - \hat{y}_e \quad (29)$$

when a measurement arrives. To formulate the sensor output matrix  $H$  and measurement noise matrix  $R$ , a theoretical expression for the measurement residual must be determined in terms of the error state. In this case, an expression for  $\delta\eta_2$  in terms of  $\delta\rho$  must be found. This formulation is similar to the relationship between the Euler attitude rates and platform angular rates. Quantity  $\delta\eta_2$  describes attitude error relative to the intermediate rotation axes  $(\hat{i}_1, \hat{j}_2, \hat{k}_3)$ , while  $\delta\rho$  describes attitude error in tangent frame  $(\hat{i}_t, \hat{j}_t, \hat{k}_t)$ . By definition,

$$\begin{aligned}\delta\rho &= \delta\phi\hat{i}_1 + \delta\theta\hat{j}_2 + \delta\psi\hat{k}_3 \\ &= \delta\phi(c\theta c\psi\hat{i}_t + c\theta s\psi\hat{j}_t - s\theta\hat{k}_t) - \delta\theta(s\psi\hat{i}_t - c\psi\hat{j}_t) + \delta\psi\hat{k}_t \\ &= (\delta\phi c\theta c\psi - \delta\theta s\psi)\hat{i}_t + (\delta\phi c\theta s\psi + \delta\theta c\psi)\hat{j}_t + (\delta\psi - \delta\phi s\theta)\hat{k}_t \\ &= \Sigma\delta\eta_2,\end{aligned}$$

where

$$\Sigma = \begin{bmatrix} c\theta c\psi & -s\psi & 0 \\ c\theta s\psi & c\psi & 0 \\ -s\theta & 0 & 1 \end{bmatrix}.$$

The theoretical measurement error expression is therefore

$$\begin{aligned}\delta y_e &= \{\eta_2 + n_e\} - \{\hat{\eta}_2\} \\ &= \Sigma^{-1}\delta\rho + n_e \\ &= H\delta x + n_e,\end{aligned}$$

where the sensor output matrix is

$$H = [ 0 \quad \Sigma^{-1} \quad 0 \quad 0 \quad 0 \quad 0 ]. \quad (30)$$

Note that  $\Sigma^{-1}$  approaches a singularity as  $\theta \rightarrow \pm\frac{\pi}{2}$ . The measurement noise matrix is

$$\begin{aligned}R &= E \langle \delta y \delta y^\top \rangle \\ &= E \langle n_e n_e^\top \rangle \\ &= \sigma_e^2 I,\end{aligned} \quad (31)$$

which is positive definite for all time. Quantities  $H\delta x$  and  $R$  represent the mean and covariance, respectively, of the distribution for  $\delta y$ . When an attitude measurement arrives, the Kalman filter evaluates equations (29)–(31) and then uses the results in (8)–(12), and (28a)–(28c) to correct the state estimate. Note that the Kalman filter assumes  $\delta\rho$  is small; therefore, the attitude sensor should initialize  $\hat{\eta}_2$  with the latest measurement when the filter initializes. In Section 4.1, we show that yaw is observable from the long baseline system when the vehicle has a nonzero velocity, thus the magnetic compass can be disabled if necessary.

### 3.6.2 Doppler Velocity Log Update

The Doppler velocity log (DVL) measures velocity via the Doppler effect by first emitting encoded acoustic pulses from each of its four transducer heads. These pulses reflect off surfaces, such as the seafloor, and return back to each transducer. The instrument measures the change in frequency between the pulses emitted and those received, which relates to velocities along each

beam direction relative to the reflecting object. In certain situations, one or more beams may not return valid information. When fewer than three beams return valid information, we cannot compute geometric transformation [14] to relate beam velocities to instrument frame velocities. It is possible to alleviate this restriction. Here, we treat each beam velocity as a separate innovation. This approach does not require *bottom lock* and incorporates more information into the filter than an instrument frame correction (i.e., four beam corrections vs. three orthogonal corrections).

Let  $b = \{b_1, b_2, b_3, b_4\}$  be unit vectors along each beam direction. The  $i$ th Doppler measurement is

$$y_v = (\nu_1 + \nu_2 \times \ell_i) \cdot b_i + n_v,$$

which represents the instrument frame velocity along beam direction  $b_i$ . Vector  $\ell_i$  is the transducer head offset from the origin of the platform frame, and  $n_v$  is sensor noise with normal distribution  $N(0, \sigma_v^2)$ . The measurement estimate is therefore

$$\hat{y}_v = (\hat{\nu}_1 + \hat{\nu}_2 \times \ell_i) \cdot b_i,$$

where  $\ell_i$  and  $b_i$  are known exactly, with residual

$$\begin{aligned} \delta y_v &= y_v - \hat{y}_v \\ &= \{(\nu_1 + \nu_2 \times \ell_i) \cdot b_i + n_v\} - \{(\hat{\nu}_1 + \hat{\nu}_2 \times \ell_i) \cdot b_i\} \\ &= b_i^\top \delta \nu_1 + b_i^\top [\ell_i \times] \delta b_g + b_i^\top [\ell_i \times] \delta n_g + n_v. \end{aligned} \tag{32}$$

The sensor output matrix is

$$H = \begin{bmatrix} 0 & 0 & b_i^\top & 0 & b_i^\top [\ell_i \times] & 0 \end{bmatrix}, \tag{33}$$

and the measurement noise matrix is

$$\begin{aligned} R &= E \left\langle \left\{ b_i^\top [\ell_i \times] n_g + n_v \right\} \left\{ b_i^\top [\ell_i \times] n_g + n_v \right\}^\top \right\rangle \\ &= b_i^\top [\ell_i \times] \sigma_g^2 I [\ell_i \times]^\top b_i + \sigma_v^2, \end{aligned} \tag{34}$$

which is positive definite for all time. Note the significance of the sensor placement in relation to the gyro bias and variance. Offset  $\ell_i$  provides observability to the gyro bias in equation (33), while  $\ell_i^2$  magnifies the effect of the gyro variance in equation (34). We ignore any correlation between the process noise  $n_g$  and measurement noise vectors. When a DVL beam measurement arrives, the Kalman filter evaluates equations (32)–(34) and then uses the results in (8)–(12), and (28a)–(28c) to correct the state estimate. Each beam provides a separate measurement correction.

### 3.6.3 Long Baseline Update

The acoustic long baseline (LBL) system precisely measures the time of flight of sound waves propagating through water. At time  $t_0$ , the vehicle transceiver generates a common interrogate ping. Each listening transponder hears this ping, each at a different time, then waits a specified turn-around time and responds. For example, transponder 1 responds 250 ms after hearing the ping, transponder 2 responds at 500 ms, followed by transponder 3 at 750 ms, and finally transponder 4 at 1000 ms after hearing the ping. No two transponders respond at the same time, allowing the the turn-around time to identify the transponder. The vehicle receives the response from the  $i$ th transponder at time  $t_i$ . Figure 2 illustrates the interrogation cycle.

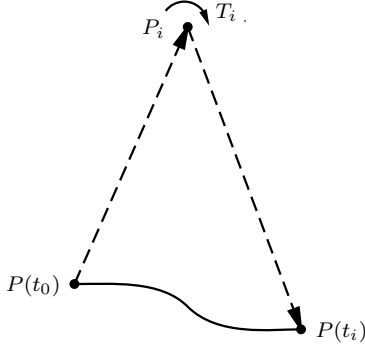


Figure 2: Long baseline interrogation cycle. Dotted lines indicate the acoustic measurement. The solid line indicates an arbitrary vehicle trajectory.

The total round-trip time for the  $i$ th transponder measurement is the travel time to the transponder plus the return travel time plus the turn-around time plus noise, or

$$y_t = \frac{1}{c(t_0)} \|P_i - P(t_0)\| + \frac{1}{c(t_i)} \|P_i - P(t_i)\| + T_i + n_t,$$

where  $c(t)$  is the speed of sound in seawater and position vectors  $P_i$  and  $P(t)$  represent the position of transponder  $i$  and the vehicle transceiver at time  $t$ , respectively. The vehicle transceiver position in tangent frame is  $P = \eta_1 + R_p^t \ell$ , where  $\ell$  is the sensor offset from the platform origin. Constant  $T_i$  is the transponder turn-around time. Sensor noise  $n_t$  is distributed according to  $N(0, \sigma_t^2)$ . The measurement estimate is therefore

$$\hat{y}_t = \frac{1}{\hat{c}(t_0)} \|P_i - \hat{P}(t_0)\| + \frac{1}{\hat{c}(t_i)} \|P_i - \hat{P}(t_i)\| + T_i,$$

where the transponder position  $P_i$  and turn-around time  $T_i$  are known. The algorithm stores the current state estimate at time  $t_0$ , then recalls it to compute measurement residual

$$\delta y_t = y_t - \hat{y}_t \tag{35}$$

at time  $t_i$ . We address the nonlinear 2-norm expression  $d(t) = \frac{1}{c(t)} \|P_i - P(t)\|$  by representing it using a first-order Taylor series approximation about state estimate  $\hat{x}$ ,

$$\begin{aligned} d &= \hat{d} + \frac{\partial d}{\partial x^\top} \Big|_{\hat{x}} (x - \hat{x}) + \frac{1}{2!} \frac{\partial^2 d}{(\partial x^2)^\top} \Big|_{\hat{x}} (x - \hat{x})^2 + \dots \\ &\approx \hat{d} + \frac{\partial d}{\partial x^\top} \Big|_{\hat{x}} \delta x. \end{aligned}$$

The dependence on state estimates at two separate times complicates the formulation of the measurement residual. It is necessary to relate the error state backwards in time to the common interrogate ping via state transition matrix  $\Phi(t_0, t_i)$ . The measurement residual is then

$$\begin{aligned} y_t &= \left\{ d(t_0) + d(t_i) + T_i + n_t \right\} - \left\{ \hat{d}(t_0) + \hat{d}(t_i) + T_i \right\} \\ &= \left[ d(t_0) - \hat{d}(t_0) \right] + \left[ d(t_i) - \hat{d}(t_i) \right] + n_t \\ &\approx \frac{\partial d(t_0)}{\partial x^\top} \Big|_{\hat{x}(t_0)} \delta x(t_0) + \frac{\partial d(t_i)}{\partial x^\top} \Big|_{\hat{x}(t_i)} \delta x(t_i) + n_t \\ &= \left[ D(t_0) \Phi(t_0, t_i) + D(t_i) \right] \delta x(t_i) + n_t, \end{aligned}$$

where the sensor output matrix is

$$H = D(t_0)\Phi(t_0, t_i) + D(t_i). \quad (36)$$

State transition matrix  $\Phi(t_0, t_i)$  propagates the error state backwards in time from time  $t_i$  to  $t_0$ . At each time step, from time  $t_0$  to  $t_i$ , the time propagation routine accumulates transition matrix  $\Phi(t_i, t_0)$  according to  $\Phi(t + \Delta t, t_0) = \Phi(t + \Delta t, t)\Phi(t, t_0)$ , where  $\Phi(t + \Delta t, t)$  is given by equation (24). When a measurement arrives, the measurement correction routine computes the inverse relationship, where  $\Phi(t_0, t_i) = \Phi^{-1}(t_i, t_0)$ , and applies the measurement correction. The nonzero partial derivative terms of matrix  $D(t)$  are

$$\begin{aligned} \left. \frac{\partial d(t)}{\partial \eta_1^\top} \right|_{\hat{x}} &= -\frac{1}{\hat{c}(t)} \frac{(P_i - \hat{P}(t))^\top}{\|P_i - \hat{P}(t)\|} \\ \left. \frac{\partial d(t)}{\partial \rho^\top} \right|_{\hat{x}} &= \frac{1}{\hat{c}(t)} \frac{(P_i - \hat{P}(t))^\top}{\|P_i - \hat{P}(t)\|} [\hat{R}_p^t(t)\ell \times] \\ \left. \frac{\partial d(t)}{\partial c} \right|_{\hat{x}} &= -\frac{1}{\hat{c}^2(t)} \|P_i - \hat{P}(t)\|. \end{aligned}$$

The measurement noise matrix is

$$R = E \langle n_t n_t^\top \rangle = \sigma_t^2, \quad (37)$$

which is a positive scalar for all time. When the vehicle transceiver emits a common interrogate ping, the correction routine stores the current state estimate, while the time propagation routine begins accumulating the state transition matrix. During this time, the filter does not correct the navigation state according to equation (12) until the last transponder measurement arrives. This practice is necessary such that we can relate  $\delta x(t_i)$  to  $\delta x(t_0)$  via  $\Phi(t_0, t_i)$ . All intermediate corrections, including those from other aiding sensors, propagate in  $\delta x^-$ . When a measurement arrives, the Kalman filter evaluates equations (35)–(37) and then uses the results in equations (8)–(11) to correct the error state. When the last transponder measurement arrives, the filter corrects the navigation state according to equation (12) and equations (28a)–(28c). Timeout logic is necessary to handle the situation where the last measurement does not arrive. After all transponders reply or timeout, the cycle repeats. To ensure stability during the initialization process, we initialize diagonal elements of  $P_{0|0}$  relating to  $\delta \eta_1$  and  $\delta c$  artificially small.

### 3.6.4 Pressure Update

Over the vehicle's operating depths, the Saunders and Fofonoff (1976) relationship [15] between pressure and depth is nearly linear, thus we model the pressure sensor as

$$y_z = s(\eta_1 + R_p^t \ell) + b_z + n_z,$$

where  $s$  and  $b_z$  scale and offset the pressure measurement, respectively, and  $s = [0, 0, s_z]$ . Vector  $\ell$  is the sensor position in platform frame. Sensor noise  $n_z$  is distributed according to  $N(0, \sigma_z^2)$ . The measurement prediction is then

$$\hat{y}_z = s(\hat{\eta}_1 + \hat{R}_p^t \ell) + b_z,$$

where we assume constants  $s_z$  and  $b_z$  are known. Therefore, the residual can be calculated as

$$\begin{aligned} \delta y_z &= y_z - \hat{y}_z \\ &= \{s(\eta_1 + R_p^t \ell) + b_z + n_z\} - \{s(\hat{\eta}_1 + \hat{R}_p^t \ell) + b_z\} \\ &= s\delta \eta_1 - s[\hat{R}_p^t \ell \times] \delta \rho + n_z. \end{aligned} \quad (38)$$

The sensor output matrix is then

$$H = \begin{bmatrix} s & -s[\hat{R}_p^t \ell \times] & 0 & 0 & 0 & 0 \end{bmatrix} \quad (39)$$

with a measurement noise matrix of

$$R = E \left\langle n_z n_z^\top \right\rangle = \sigma_z^2, \quad (40)$$

which is a positive scalar for all time. When a pressure measurement arrives, the Kalman filter evaluates equations (38)–(40) and then uses the results in equations (8)–(12), and equations (28a)–(28c) to correct the state estimate.

## 4. ANALYSIS

To analyze our filter implementation, we examine the navigation state error, covariance, and measurement residuals. Here, we consider several scenarios in simulation and study the navigation state error and covariance. In Section 5, we evaluate the measurement residuals for experimental data. The navigation state error  $\tilde{x}$ , which is only available when the true navigation state is available, substantiates the filter’s performance. The objective is to drive the navigation state error to zero. The covariance matrix provides a performance estimate of  $\delta x$ , where the square root of the diagonal describes the error state standard deviation. We expect the navigation state error to remain within three standard deviations of zero. The measurement residuals describe the performance of the filter’s measurement predictions. These residuals should be white noise when the system and measurement models approximate the true system.

The vehicle simulation is comprehensive. It models a three-dimensional environment, sensor performance, vehicle dynamics, and executes the actual vehicle software to approximate real-world performance. The sensor models are similar to those presented above, where in addition to measurement noise, we incorporate sporadic sensor dropouts and those due to poor geometry and loss of line of sight. Acoustic sensor models are simple. We do not attempt to model acoustic sound propagation or multi-path effects, and we assume that acoustic transmissions are instantaneous with respect to the simulation step size. The vehicle model accounts for vehicle dynamics, hydrodynamics, currents, and thruster forces based on experimental data. For analysis purposes, we assume this model represents the truth model.

It is helpful to understand the observability of the system for analysis. Observability analysis allows one to determine if it is possible to estimate the error state  $\delta x$  from the output  $y$ . Given system matrix  $F$  and a measurement output matrix  $H$ , we can compute observability matrix  $\mathcal{O}$  to determine the states made observable via the measurement correction associated with  $H$ . Unobservable states may remain constant or diverge, depending on the model and time propagation routine. The rate of divergence deserves future discussion. To check observability, construct the observability matrix

$$\mathcal{O} = \begin{bmatrix} H \\ HF \\ \vdots \\ HF^{n-1} \end{bmatrix},$$

where matrix  $H$  is a measurement output matrix or combination of multiple measurement output matrices  $H = [H_1^\top, H_2^\top, \dots]^\top$ . The rank of  $\mathcal{O}$  indicates the number of error states observable; if

$\mathcal{O}$  is full rank, we can estimate the entire error state from output  $y$  [7, 8]. The dimension of our system is 16, thus a rank of 16 is necessary to estimate  $\delta x$ . The rank of  $\mathcal{O}$  is complementary to the dimension of the unobservable subspace. Clearly,  $\mathcal{O}$  depends on  $x$  for nonlinear systems. We assume nominal conditions ( $\hat{x} = [0, 0, 0, 0, 0, 1500]^\top$ ) unless stated.

The scenarios of interest are where different combinations of acoustic sensors drop out. These sensors, which include the LBL and DVL, are highly susceptible to interference, so it is important to examine the effect when their respective measurements are unavailable. For each scenario, the vehicle submerges to 5 m in depth, and then executes a lawnmower search pattern. The leg length is 40 m, with a row spacing of 5 m. After nine consecutive rows, the vehicle returns to the beginning of the first row and repeats the mission. The vehicle speed is 0.5 m/s. The acoustic baseline outlines a  $50 \times 50 \text{ m}^2$  box around the operating area. Figure 3 illustrates the mission trajectory. The true initial conditions are normally distributed about zero with realistic variances, except for the vehicle yaw angle and the speed of sound. Yaw is uniformly distributed about a circle, and speed of sound is normally distributed about 1450 m/s with variance  $(15 \text{ m/s})^2$ . All initial estimates are zero or the first available measurement, except for the speed of sound, which is 1500 m/s. For the nominal case, the system has full observability, thus we expect to estimate  $\delta x$  and therefore  $x$  when all sensors are functioning.

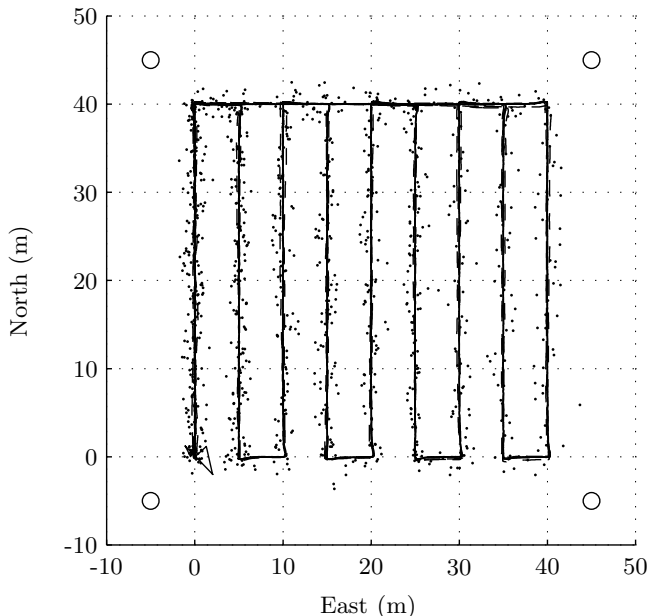


Figure 3: North–East plot of one simulated mission from the incremental LBL dropout scenario, where the solid line represents the navigation estimate and the dashed line represents the true trajectory. The four circles represent the LBL transponders. For comparison, the small dots represent three and four-range trilateration solutions.

All results represent the average of 100 Monte Carlo simulations. The error plots illustrate the true navigation state error  $\tilde{x}$  and the corresponding standard deviation estimate of  $\delta x$  (divided by 10). All  $\delta x$  divergence rates are for one standard deviation. Our observability analysis assumes  $\omega_{i/e} \approx 0$  to eliminate the attitude observability gained from the rotation of the Earth.

#### 4.1 INCREMENTAL LBL DROPOUTS, LIMITED COMPASS AIDING

First, consider the ship-hull inspection scenario. Operators place one LBL transponder at each corner of a ship and deploy an inspection vehicle. The vehicle executes several passes around and underneath the hull, searching for objects of interest. In this scenario, the keel frequently obstructs line of sight between the vehicle and one or more transponders, and, due to magnetic anomalies, vehicles typically operate without a magnetic compass. To illustrate the system performance in this scenario, we sequentially drop out LBL transponders. Transponder one fails at 600 seconds, followed by transponders two, three, and four at 1200, 1800, and 2400 seconds, respectively. Yaw aiding is only available during the first 30 seconds of the mission, which allows the algorithm to estimate  $\eta_2$  such that  $\delta\rho$  becomes small before disabling the compass. The DVL, pressure, and inclinometers continue to aid the system. Figures 4, 5, and 6 illustrate the performance of the east position, azimuth, and speed of sound error states, respectively.

On interval  $t \in [30, 600)$  seconds, where four transponders are responding and the compass is disabled, the nominal system has  $\text{rank}(\mathcal{O}) = 15$ . The unobservable subspace  $\Sigma_u$  spans linear combinations of  $\{\delta\eta_1(x, y), \delta\rho(\psi)\}$ . This result is intuitive. Clearly, we cannot observe azimuth when the vehicle is stationary. Observability analysis indicates that velocity in the horizontal direction promotes  $\mathcal{O}$  to full rank; vertical velocity does not. Vehicle rotation, where  $\nu_2(r) \neq 0$ , also promotes  $\mathcal{O}$  to full rank.

The loss of one transponder does not affect the observability of the nominal system. The unobservable subspace remains unchanged. Velocity in the horizontal direction promotes  $\mathcal{O}$  to full rank. Rotating, however, does not promote  $\mathcal{O}$  to full rank. The unobservable subspace transforms where linear combinations of  $\{\delta\eta_1(x, y), \delta\rho(\psi), \delta c\}$  are not observable. Eliminating  $\delta c$  from the error state vector allows this maneuver to achieve full observability.

Losing two transponders increases the dimension of  $\Sigma_u$  to 2, where  $\Sigma_u$  spans linear combinations of  $\{\delta\eta_1(x, y), \delta\rho(\psi), \delta c\}$ . Velocity in the horizontal direction no longer achieves full observability. The algorithm cannot differentiate between certain linear combinations of  $\delta\eta_1(x, y)$  and  $\delta c$ . To im-

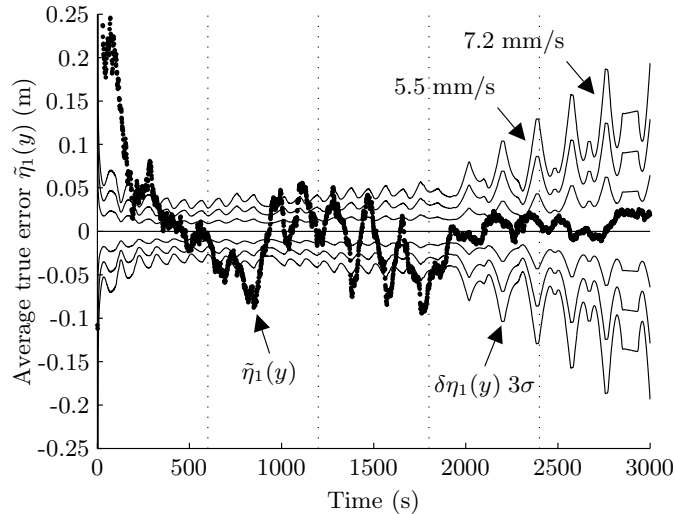


Figure 4: East position error  $\tilde{\eta}_1(y)$  for incremental LBL transponder dropouts and limited compass aiding. LBL transponders drop out at multiples of 600 seconds. The oscillations in standard deviation correlate to the vehicle trajectory and its relationship to each transponder.

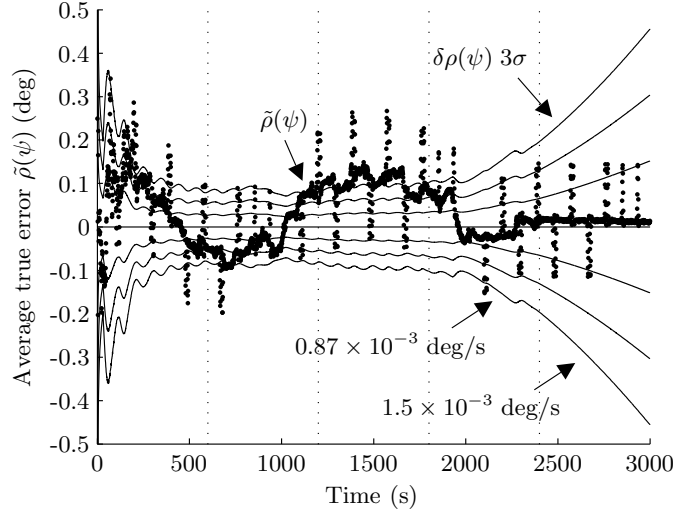


Figure 5: Azimuth error  $\tilde{\rho}(\psi)$  for incremental LBL transponder dropouts and limited compass aiding. LBL transponders drop out at multiples of 600 seconds. The true azimuth error is computed using equation (19a).

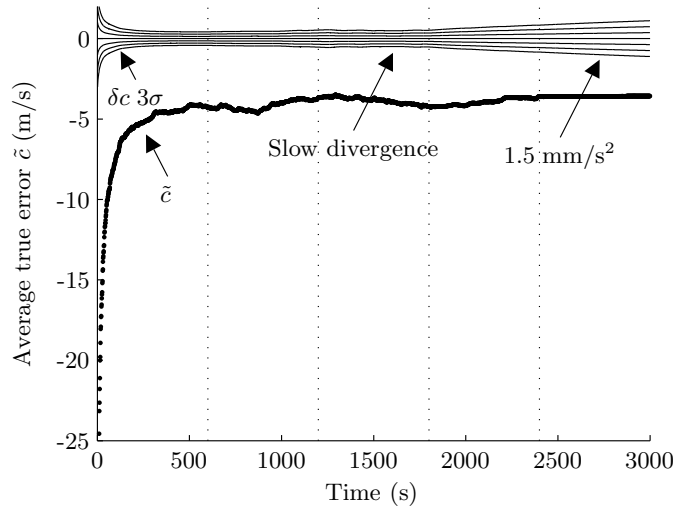


Figure 6: Sound speed error  $\tilde{c}$  for incremental LBL transponder dropouts and limited compass aiding. LBL transponders drop out at multiples of 600 seconds.

prove results, one could invest in aiding sensors for  $\delta c$  or assume the speed of sound is deterministic. Elimination of  $\delta c$  from the error state vector makes  $\mathcal{O}$  full rank for nonzero horizontal velocities. For small operating regions, assuming a constant sound speed may produce acceptable results. Figure 6 shows that the covariance of  $\delta c$  converges prior to the loss of the second transponder. Since the driving noise is small, the Kalman gain  $K$  is small and the estimate remains steady over interval  $t \in [1200, 1800)$  seconds.

The loss of the third transponder results in divergence. Figures 4 and 5 indicate the divergence rates for east position error and azimuth error, respectively. On interval  $t \in [1800, 2400)$  seconds, where only one transponder operates,  $\text{rank}(\mathcal{O}) = 13$  for zero velocity and  $\Sigma_u$  spans linear combinations of  $\{\delta\eta_1(x, y), \delta\rho(\psi), \delta c\}$ . For nonzero horizontal velocities,  $\text{rank}(\mathcal{O}) = 14$  and  $\Sigma_u$  spans linear

combinations of  $\{\delta\eta_1(x, y), \delta c\}$ . Losing all transponders reduces observability to 11 states and  $\Sigma_u$  spans linear combinations of  $\{\delta\eta_1(x, y), \delta\rho(\psi)\}$ ,  $\{\delta b_g(\psi)\}$ , and  $\{\delta c\}$ .

Note that as  $\|P_i - \hat{P}(t)\| \rightarrow 0$  in equation (36),  $\delta c$  becomes weakly observable. Thus, for small area searches such as the scenario presented here, the algorithm may be unable to estimate  $\delta c$  accurately as a result of the LBL sensor performance characteristics. We assume  $\sigma_t = 1.0$  ms and  $\sigma_c = 0.1$  m/s. Figure 6 shows that we cannot estimate the true speed of sound within 5 m/s for the given scenario.

## 4.2 INCREMENTAL DVL BEAM DROPOUTS, NO LBL AIDING

Consider the scenario when the LBL sensor is unavailable and the DVL begins to malfunction. Beam one fails at 200 seconds, followed by beams two, three, and four at 400, 600, and 800 seconds, respectively. The attitude and pressure sensors continue to aid the system. Figures 7 and 8 depict the performance of velocity error  $\tilde{\nu}_1(u)$  and accelerometer bias error  $\tilde{b}_a(u)$ . Initially, the north and east error states, as well as the speed of sound, are not observable, and  $\text{rank}(\mathcal{O}) = 13$ . The unobservable subspace spans linear combinations of  $\{\delta\eta_1(x, y)\}$  and  $\{\delta c\}$ . This result is expected since no sensors aid position or speed of sound. When beam one fails, there is no additional loss in observability. Subspace  $\Sigma_u$  transforms, but the general relationships remain the same. Figure 7 shows only a slight decrease in performance.

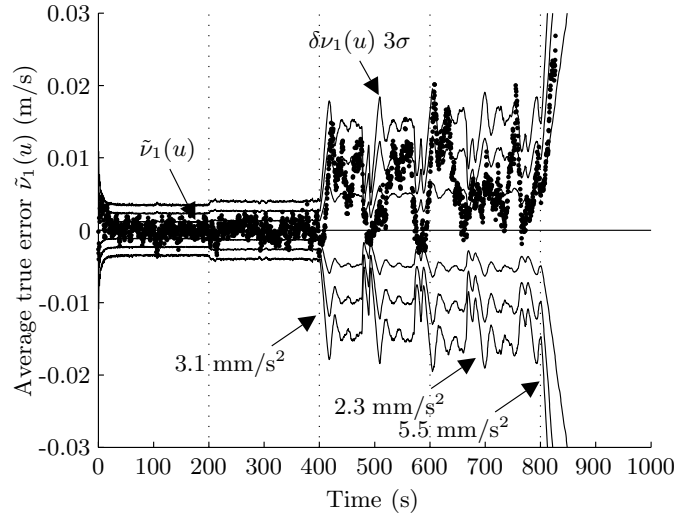


Figure 7: Velocity error  $\tilde{\nu}_1(u)$  for incremental DVL beam dropouts and no LBL aiding. DVL beams drop out at multiples of 200 seconds.

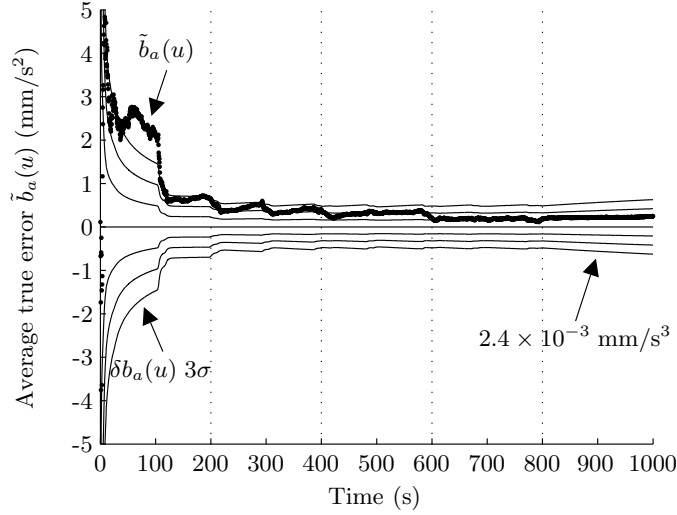


Figure 8: Accelerometer bias error  $\tilde{b}_a(u)$  for incremental DVL beam dropouts and no LBL aiding. DVL beams drop out at multiples of 200 seconds.

The performance resulting for a loss of a second beam depends on the particular beam lost. If the remaining beams lie within perpendicular planes, the unobservable subspace remains the same dimension and the performance loss is subtle. If the remaining beams lie within the same plane, the effect is detrimental. Our simulation reveals this condition, where the dimension of  $\Sigma_u$  increases to 5 and the rank of  $\mathcal{O}$  drops to 11. Linear combinations of  $\{\delta\eta_1(x, y), \delta\nu_1, \delta b_a\}$  and  $\{\delta c\}$  are not observable. From Figure 7, we see that sometimes the system excites observable modes and the error state and covariance briefly converge. To understand this behavior, we perform a separate observability analysis for different conditions.

For nonzero velocity, such as when the vehicle is tracking the segment between two waypoints,  $\Sigma_u$  has dimension 5. For nonzero angular rates, such as when the vehicle achieves a waypoint and maneuvers towards the next waypoint,  $\Sigma_u$  has dimension 4. Linear combinations of  $\{\delta\eta_1(x, y), \delta\nu_1, \delta b_a\}$  and  $\{\delta c\}$  are not observable for both cases. Finally, when the vehicle has a nonzero roll or pitch angle,  $\Sigma_u$  has dimension 3. For this condition, the unobservable subspace is similar to a single beam failure. The oscillations in Figure 7 correspond to the trajectory of the vehicle. At each waypoint, the vehicle maneuvers (with nonzero angular rates, and a slight roll angle) towards the next waypoint and the solution converges. When tracking the segment between two waypoints, the solution diverges. Losing a third beam is similar to the previous case, where the dimension of  $\Sigma_u$  is 5. The performance loss is subtle over interval  $t \in [600, 800)$ . The divergence rates are comparable to a two-beam failure.

A total loss of the DVL causes divergence rates to increase. The divergence rate corresponding to velocity error  $\delta\nu_1(u)$  is  $5.5 \text{ mm/s}^2$  and to accelerometer bias error  $\delta b_a(u)$  is  $2.4 \times 10^{-3} \text{ mm/s}^3$ . The rank of  $\mathcal{O}$  drops to 9 states, and the system can no longer maintain an acceptable level of performance. Note that this scenario illustrates the worst case. Intermittent beam dropouts result in only a slight decrease in performance due to an effective lower update rate.

## 5. EXPERIMENTAL RESULTS

The following experimental results are from a demonstration at the Autonomous Underwater Vehicle Festival (AUVFest) in 2007. The mission plan was to submerge to 3 m in depth for 2 minutes, then execute two sets of three-dimensional waypoints at 1 knot. The first series of waypoints consisted of vertically stacked legs between two waypoints. During this phase, the navigational goal was to observe the unknown parameters (yaw and biases) before proceeding to the second series of waypoints underneath a barge. The second series of waypoints consisted of a lawnmower search pattern in a continuous loop, similar to the scenario presented in Section 4. Due to severe magnetic interference from the barge, we chose to operate the vehicle without aiding the yaw angle with the magnetic compass. The acoustic baseline outlines a  $36 \times 9 \text{ m}^2$  box around the second series of waypoints. Since the true state is not available, we present analysis of select error state covariances and measurement residuals. Note that the sensor data presented here is identical to that presented in reference [4]; however, here we reprocessed the raw data through the algorithms presented in this report.

Position accuracy is a critical metric for inspection-class vehicles. This information allows operators to localize objects of interest, reacquire contacts, and navigation through complex environments. Figure 9 illustrates the estimated standard deviation of the north, east, and down error states during the AUVFest demonstration. These results are consistent with the simulation results in Figure 4. The convergence is dependent on the acoustic baseline geometry, vehicle trajectory, and several important factors. These factors include accuracy of the baseline calibration, estimate of the speed of sound, and the estimate of the vehicle attitude.

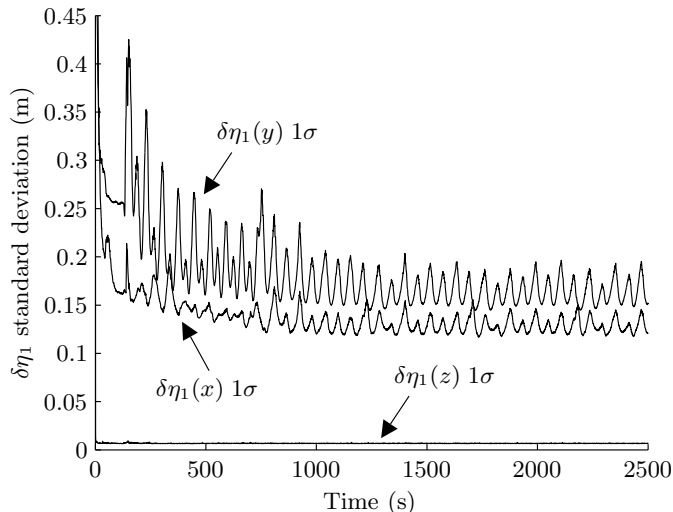


Figure 9: North, east, and down position error  $\delta\eta_1$  standard deviation. The standard deviation estimate converges to 13 cm, 17 cm, and 0.7 cm for north, east, and down position errors, respectively. These results are subject to the baseline configuration and do not necessarily mean  $\hat{\eta}_1$  is this accurate.

We determine the acoustic baseline geometry prior to deployment via acoustic calibration. Using a spare transponder, the calibration algorithm measures round-trip travel times to each transponder and among all transponders. The algorithm assumes the relative organization of transponders to formulate a geometric solution, which provides estimates for the transponder locations and the speed of sound. For our demonstration, it estimated a sound speed of 1491 m/s. The transponder

locations are in a local coordinate system, where transponder 1 identifies the origin and the vector from transponder 1 to transponder 3 defines the  $y$ -axis. We transform these coordinates into tangent plane coordinates for navigation. The current hardware implementation requires us to perform this procedure prior to operating the vehicle. It is not possible to estimate the baseline online with our current hardware. Clearly, a poor baseline calibration will degrade performance.

Analyzing the LBL round-trip measurement residuals provides insight into the baseline calibration. Figure 10 represents the measurement residuals for transponder 1. Several features are apparent. First, the residuals do not resemble white noise. Second, approximately 7 percent of the data lies beyond three standard deviations of its expected value. We attribute these erroneous measurements to acoustic noise and multi-path effects. Simple filtering techniques tend to produce inconsistent results due to the slow update rate and position uncertainty. Our current algorithm assumes all measurements are valid. Another notable feature evident in the data is a profound oscillation. This oscillation is evident in all transponder residuals and is consistent with a poor baseline calibration in simulation. Simulation results confirm that misalignment of one transponder will hinder performance of the entire system. The oscillation correlates to the vehicle trajectory. Figure 9 also shows an oscillatory pattern in the north and east error state standard deviations.

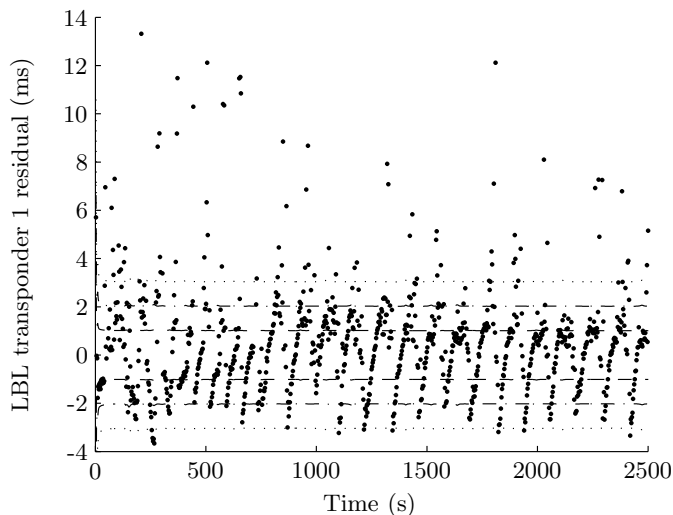


Figure 10: Long baseline transponder 1 residual. This residual exhibits an oscillatory pattern that is consistent with baseline misalignment and the vehicle trajectory. All transponder residuals exhibit similar patterns. The horizontal lines indicate one, two, and three standard deviations about zero, where  $\sigma = \sqrt{HP^{-1}H^T + R}$ .

Inaccuracies in the speed of sound estimate can also cause oscillations in the round-trip measurement residuals. Figure 11 illustrates the estimate of the speed of sound. The calibration routine estimated 1491 m/s. The navigation algorithm, however, converged near 1420 m/s, which is unrealistic, given environmental conditions. Possible explanations include unknown biases, scale factors, and inaccuracies in the sensor clock frequency.

The azimuth error is of particular interest since yaw is an essential control signal and  $\delta\rho(\psi)$  is only observable via the long baseline system. Poor estimation of error state  $\delta\rho(\psi)$ , and  $\delta\rho$ , generally, will result in inadequate navigation and control performance. Figure 12 illustrates the azimuth and corresponding gyro bias error standard deviations. The azimuth error  $\delta\rho(\psi)$  standard deviation converges to 0.5 deg. This result does not necessarily mean  $\hat{\rho}(\psi)$  is this accurate, however, it is consistent with the simulation results in Figure 5. Note that the performance specifications for our

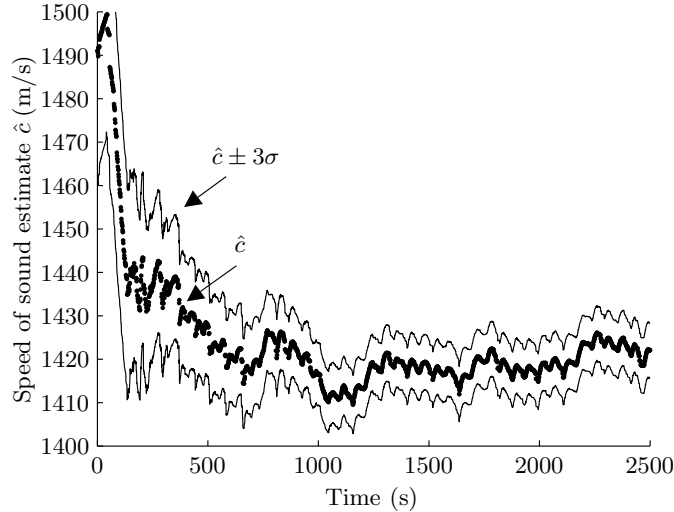


Figure 11: Sound speed estimate  $\hat{c}$ . Thin lines indicate three standard deviations beyond the estimate. The estimate converges to approximately 1420 m/s, which is suspicious, given the environmental conditions.

fiber-optic gyro include a bias stability of  $<20$  deg/hr and random walk of  $<0.4$  deg/hr $^{\frac{1}{2}}$ .

Estimation of the unknown accelerometer and gyro bias parameters is a key aspect of our approach. Poor estimation of these parameters leads to inaccuracies in the time propagation of the navigation state vector, and thus poor measurement predictions for the aiding sensors. Figure 13 illustrates the convergence of the unknown bias parameters. All parameters converged to reasonable values within the first 500 seconds. The convergence rate is subject to the aiding sensors.

Figure 14 illustrates the measurement residuals for DVL beam 1. Initially, the residuals are noisy as the estimates for platform velocity, attitude, and biases estimates are converging. After the filter reaches steady state, the residuals resemble white noise. Residuals beyond three standard deviations are ignored.

## 6. FUTURE WORK

The experimental results indicate that inaccuracies in the acoustic baseline will degrade performance. The algorithm presented in this article does not attempt to estimate the individual transponder locations, nor does it account for uncertainty in the baseline. To improve results, it may be necessary to estimate the baseline as well as unknown parameters, such as the clock scale factors and biases. Recent advancements in acoustic baseline sensor capabilities permit more sophisticated algorithms. These capabilities include baseline measurements via acoustic relaying, Doppler shift measurements, and bearing measurements. It is also possible to communicate information among acoustic nodes.

Baseline measurements via acoustic relaying provide travel time measurements between transponders. This information permits integrating calibration routines into the navigation algorithms. Consider the following measurement cycle, where the objective is to obtain an estimate of the travel time between transponders  $A$  and  $B$ . To initiate the cycle, the vehicle  $V$  interrogates  $A$  for the travel time between  $A$  and  $B$ . Transponder  $A$  receives this request from  $V$ , waits a known turn-around time, then interrogates  $B$ . Transponder  $B$  receives this request from  $A$ , waits a known turn-around

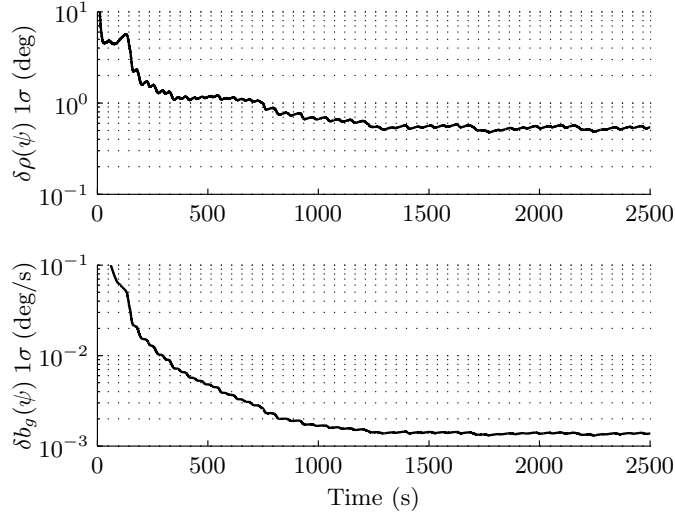


Figure 12: Semi-log plots of azimuth and gyro bias error standard deviations. Azimuth error  $\delta\rho(\psi)$  standard deviation converges to 0.5 deg. Gyro bias error  $\delta b_g(\psi)$  standard deviation converges to  $1.5 \times 10^{-3}$  deg/s.

time, then replies. Finally, transponder  $A$  receives the reply from  $B$ , and then transmits the travel time measurement to the vehicle after a known turn-around time. Since the vehicle can hear the communications between  $A$  and  $B$ , four pieces of information can be extracted from this measurement cycle. The vehicle obtains travel times for  $V \rightarrow A \rightarrow V$ ,  $V \rightarrow A \rightarrow B \rightarrow V$ ,  $V \rightarrow A \rightarrow B \rightarrow A \rightarrow V$ , and the direct measurement  $A \rightarrow B \rightarrow A$ . This capability allows navigation algorithms to make intelligent LBL measurement cycle decisions to optimize overall system performance. Further performance can be obtained by manipulating the turn-around times as a function of vehicle position in order to maximum the update rate.

Doppler shift measurements allow the vehicle to measure the relative velocity between the vehicle and the transponder. Unique encoding in the acoustic communications makes this capability possible. The corresponding measurement correction is similar to the correction presented in Section 3.6.2, however, in this case the measurement direction is not deterministic.

Bearing measurements are possible using an ultrashort baseline (USBL) configuration fixed to the vehicle. The USBL is a method of underwater acoustic positioning where the transceiver incorporates multiple hydrophones, all within a half-wavelength of each other. By computing the relative phase between hydrophones, the bearing of the acoustic source can be resolved. Bearing measurements are particularly attractive, as they could provide frequent measurement corrections while receiving time-consuming acoustic communications from topside.

Clearly, additional sensors and/or higher quality sensors will improve performance. In this report, we formulated a robust navigation algorithm for autonomous underwater vehicles using an error state formulation of the Kalman filter. The algorithm incorporates unique acoustic sensors, such as the Doppler velocity log and a long baseline system, and can estimate critical bias parameters to improve performance. Future work will address inaccuracies in the acoustic baseline to improve results further.

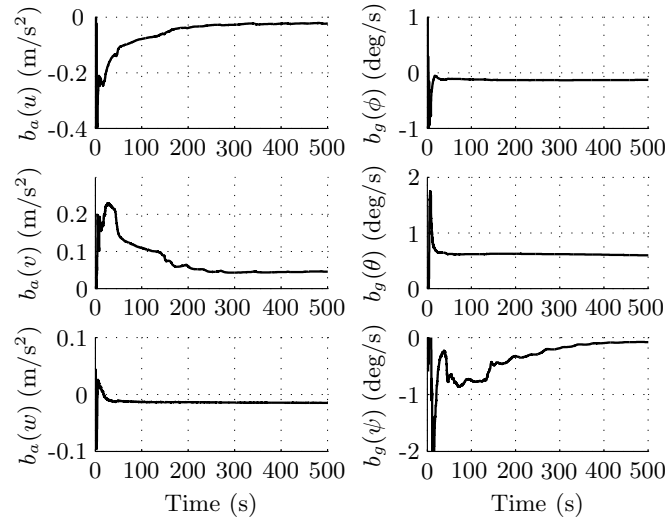


Figure 13: Accelerometer and gyro bias estimates. Biases converge to reasonable values quickly.

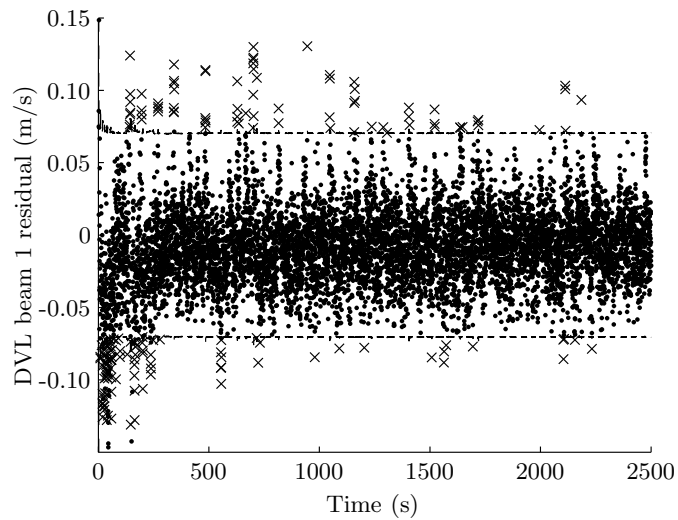


Figure 14: Doppler velocity log beam 1 residual. The dashed lines indicate three standard deviations, where  $\sigma = \sqrt{HP^{-1}H^T + R}$ . Residuals beyond three standard deviations are ignored as indicated by the  $\times$  marker.

## 7. REFERENCES

- [1] R. G. Brown and P. Y. C. Hwang, *Introduction to Random Signals and Applied Kalman Filtering with Matlab Exercises and Solutions*, 3rd ed. John Wiley and Sons Inc., 1996.
- [2] A. Gelb, *Applied Optimal Estimation*. Cambridge, MA: MIT Press, 1974.
- [3] M. S. Grewal, L. R. Weill, and A. P. Andrews, *Global Positioning Systems, Inertial Navigation, and Integration*, 2nd ed. John Wiley and Sons Inc., 2007.
- [4] P. A. Miller, Y. Zhao, V. Djapic, and J. Farrell, “Autonomous underwater vehicle navigation,” in *Proc. of 15th Int’l Symp. on Unmanned Untethered Submersibles Technologies*. Durham, NH: AUSI, August 2007.
- [5] T. I. Fossen, *Guidance and Control of Ocean Vehicles*. John Wiley and Sons Inc., 1994.
- [6] H. Baruh, *Analytical Dynamics*. New York, NY: McGraw-Hill, 1998.
- [7] W. L. Brogan, *Modern Control Theory*, 3rd ed. Upper Saddle River, NJ: Prentice-Hall, Inc., 1991.
- [8] C. Chen, *Linear System Theory and Design*, 3rd ed. New York, NY: Oxford University Press, 1998.
- [9] K. R. Britting, *Inertial Navigation Systems Analysis*. New York, NY: John Wiley and Sons Inc., 1972.
- [10] R. M. Rogers, *Applied Mathematics in Integrated Navigation Systems*, ser. AIAA Education Series. Reston, VA: American Institute of Aeronautics and Astronautics, Inc., 2000.
- [11] C. Moler and C. Van Loan, “Nineteen dubious ways to compute the exponential of a matrix,” *SIAM Review*, vol. 20, no. 4, pp. 801–836, Oct 1978.
- [12] J. A. Farrell and M. Barth, *Global Positioning System and Inertial Navigation*. New York, NY: McGraw-Hill, 1999.
- [13] J. D. Lambert, *Computational Methods in Ordinary Differential Equations*. John Wiley and Sons Inc., 1973.
- [14] RD Instruments, Inc., “ADCP coordinate transformation, formulas and calculations,” RD Instruments, Inc., San Diego, CA, P/N 951-6079-00, 1998.
- [15] P. M. Saunders and N. P. Fofonoff, “Conversion of pressure to depth in the ocean,” *Deep-Sea Research*, vol. 23, pp. 109–111, 1976.

Approved for public release; distribution is unlimited.